Results in Engineering 25 (2025) 104217

Contents lists available at ScienceDirect

Results in Engineering

journal homepage: www.sciencedirect.com/journal/results-in-engineering

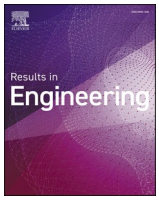

# Thermal modeling and empirical verification of multi unit small satellites

Anwar Ali [a,*], Muhammad Rizwan Mughal [b], Shoaib Ahmed Khan [c], Kar Seng Teng [a]

[a] Department of Electronic and Electrical Engineering, Swansea University Bay Campus, United Kingdom
[b] Department of Electrical and Computer Engineering, Sultan Qaboos University (SQU), Muscat, Oman
[c] College of Electrical and Mechanical Engineering, Guangzhou University, Guangzhou, China

ARTICLE INFO

*Keywords:*
Satellite
Thermal model
Thermal resistance
Multi-unit satellites

ABSTRACT

Recent developments in the miniaturization and cost reduction of small satellites have attracted the attention of researchers worldwide. The miniaturized and lightweight modular small satellites have resulted in an extensive range of multi-unit small satellites. The most challenging design aspect of the multi-unit small satellites is thermal control. In space environment, heat can be removed through conduction and radiations, because there is no heat convection, which further intensifies the need to ensure thermal stability during the design and development phases. In this paper, we present a thermal model of a small spacecraft power-management tile. Using the proposed thermal model, the thermal resistance is measured analytically for a single tile. The proposed model is applied to a single small-unit satellite structure and the resultant thermal resistance is measured. The analytically measured thermal resistances of the satellite is verified using an experimental setup. Furthermore, analytical techniques are applied to 4 U (4 units) and 8 U (8 units) multi-unit satellites. From the resultant lower value of thermal resistance, it is concluded that the heat absorbed by the spacecraft tile facing the sun is quickly dissipated to the opposite relatively cooler tile on the dark face and eventually radiates to the space environment. The proposed model is a useful tool for the preliminary design phase of a spacecraft design. By utilizing the proposed model, the designer can determine the type of material and its dimensions that can be used to obtain low thermal resistance of the spacecraft structure.

## 1. Introduction

The utilization of small satellites in general, specifically CubeSats, has seen a significant rise owing to the Newspace movement, which is different from the traditional space design approach as it lowers development, testing, launch, and operational costs and time [1,2]. Initially intended for training and educational purposes with no perceived commercial applications, the trend has changed, and the applications of nano-and microsatellites have expanded significantly in applications such as surveillance, remote sensing, navigation, space exploration, Earth observation, and scientific research [3–8]. Over the past few years, CubeSats developed in 2000 by California Polytechnic State University (Cal Poly) and Stanford University have undergone significant evolution in their commercial applications, presenting a promising future scope for commercial use [9]. With the rapid advancement in technology and innovative design approaches, there has been a great push forward in sending nanosatellite missions to even higher altitudes and deeper space [10–12]. The Department of Electronics and Telecommunication (DET) at Politecnico di Torino also contributed to small satellite projects, including AraMiS (Modular Architecture of Satellites in Italian) [13]. This project involved the development of small satellites of various dimensions and configurations [14–16].

Low Earth Orbit (LEO) satellites normally encounter many potential risks, such as high thermal gradients, radioactive space environment, lower optical pointing accuracy compared to higher orbit satellites, and complicated sensor calibrations. Higher temperature variation is usually considered one of the most important fetal elements for satellite functional and structural integrity. This can worsen the optical pointing accuracy, deteriorate sensor calibration, and result in the destruction of electronic subsystem components and battery failures. Therefore, satellite thermal control is an integral part of all spacecraft and is vital for successful missions.

In a spacecraft, heat primarily originates from instruments, heaters, or solar absorption, with radiation being the sole mechanism for heat dissipation. Thermal control includes controlling the amount of heat generation plus heat inflow and outflow from the spacecraft to ensure that the total accumulated heat inside the spacecraft remains within the

* Corresponding author.
*E-mail address:* anwar.ali@swansea.ac.uk (A. Ali).

https://doi.org/10.1016/j.rineng.2025.104217
Received 7 November 2024; Received in revised form 20 January 2025; Accepted 30 January 2025
Available online 1 February 2025

permissible limits. Spacecraft performance and the respective subsystems' lives can be prolonged when the temperature is kept within acceptable boundaries. With intensification in the subsystem's miniaturization, modularity and redundancy features, small satellites thermal control is becoming gradually more challenging which adds further to the complexity level of thermal analysis. However, there are certain techniques if they are incorporated during the design and development stages of a small satellite, the heat removal issue can be easily resolved.

When a system is immersed in space, during thermal equilibrium, the heat absorbed from the surrounding plus heat generated by the system is equal to the total heat emitted to the environment as shown in Fig. 1. In space, there is no heat convection. The heat is removed from the system only through conduction and radiation [17]. Therefore, aerospace system structures directly exposed to solar radiation have higher temperature, while the structures facing dark have very low temperature. The difference in temperature is mainly due to the higher thermal resistance between the two opposite faces. The aerospace systems with higher thermal resistance trap some portion of the absorbed and generated heats inside the structure and results in disturbing the thermal equilibrium. The trapped heat increases the satellite temperature and may cross the boundary beyond components safe temperature limit. This phenomenon may degrade the system performance and decrease the lifespan of the system components. Given the significance of thermal resistance in satellite structures, it is crucial to develop techniques for measuring and analyzing thermal resistance within an aerospace thermal environment. The spacecraft's thermal resistance is dependent on the material composition and design dimensions.

In a space thermal environment, satellite heat is usually removed by utilizing two techniques: active and passive heat control systems. The active thermal system is typically composed of heat radiators [18], shape-memory alloys (SMA) [19], and louvers [20], which require a power source, have larger dimensions, and are heavier and expensive. These attributes make active thermal heat control systems incompatible with small satellites, which usually have limited size, mass, and economic and power budgets [21]. In contrast, passive thermal control systems exploit satellite structure material conduction and radiation properties to control the temperature. Passive thermal control systems offer several advantages over active thermal control systems, primarily due to their inherent simplicity and efficiency. One of the most significant benefits of passive systems is that they do not require electric power to operate. This makes them highly desirable in spacecraft applications where power availability is limited.

Unlike active systems, which rely on powered components like pumps, fans, or heaters to regulate temperature, passive systems achieve thermal control through material properties, design strategies, and natural processes. Examples include the use of thermal insulation, radiators, phase-change materials, or heat pipes. These methods rely on principles like conduction, convection, and radiation to manage heat flow, requiring no moving parts or electrical input [22,23]. Various types of materials such as multilayer insulation, coatings, paints, mirrors, radiating surfaces, thermal greases, and polyimide structures are used for passive thermal control [24–26]. These features make passive thermal control methods the primary solution for the thermal control system of a small satellite. The efficacy of a system is determined by precise thermal analysis and effective testing [27,28].

The thermal considerations in current and future deep-space missions pose an even greater risk, as the environment is harsher than that of LEO missions. One of the critical factors to foresee when designing LEO and deepening space missions is to look at the high thermal gradients and their mitigation techniques. Several approaches have been proposed to mitigate the effects of thermal environments.

One approach involves using analytical and numerical techniques to solve the heat-transfer equations that govern the temperature distribution in a satellite. Another approach is to use empirical data from previous missions to estimate the thermal behavior of nanosatellites [29]. In [30], the authors proposed a novel thermal control system for CubeSats that utilized a phase-change material (PCM) to absorb excess heat and maintain a stable temperature. They proposed a PCM material onboard a honeycomb structure positioned near the electronic components of the nanosatellite to provide efficient thermal management. In another study [31], the authors investigated the thermal behavior of a nanosatellite with a solar panel as the main heat source. The authors developed a thermal model based on the finite element method (FEM) and simulated the temperature distribution in a nanosatellite. In [32], the authors examined the thermal behavior of nanosatellites in different orbital environments, including a Low Earth Orbit (LEO), geostationary orbit (GEO), and lunar orbit. The authors concluded that the thermal behavior of the nanosatellite was affected by the variation in solar flux and orientation of the satellite with respect to the sun. The authors in [33] proposed several simplified and detailed thermal models for small-form-factor nanosatellites.

In this study, thermal models developed for small-form-factor nanosatellites were used as a baseline and then applied to larger form factors. The paper also presents challenges and proposed solutions. Compared to previously developed models, our proposed model is simple, accurate, robust, and does not require special tools. The remainder of this paper is organized as follows. Section 2 discusses the proposed thermal model, and Section 3 discusses the thermal models of various satellite panels. In Section 4, the thermal modeling presented in Section 3 is applied to a 16.5 × 16.5 $cm^3$ dimension AraMIS satellite and

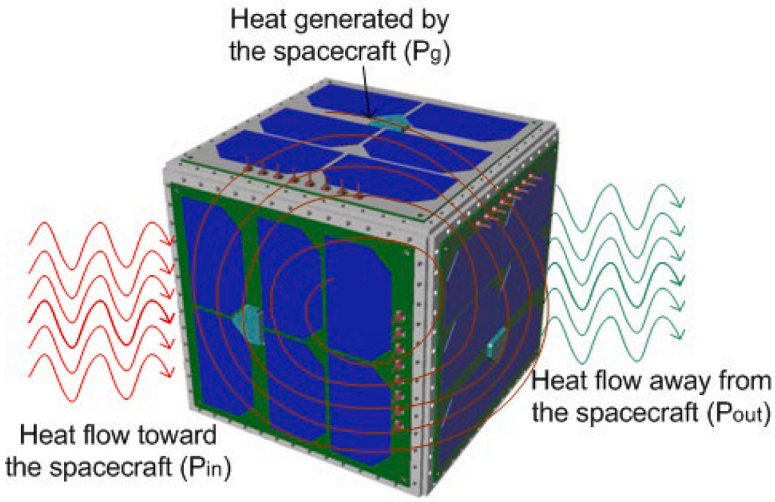


**Fig. 1.** Heat sources affecting thermal equilibrium.

its panels, and their thermal resistances are measured. In Section 5, the thermal resistances evaluated using the thermal models presented in Section 4 are verified through laboratory experiments. Finally, Section 6 concludes the study.

## 2. Proposed thermal model

A thermal model of a satellite system consisting of different materials is shown in Fig. 2. The system consists of several components with different materials connected in diverse ways, as shown in Fig. 2(a). Each component has a related thermal resistor and a capacitor. The values of the thermal resistors and capacitors depend on the material type and its physical dimensions. The thermal resistance of a specific material is given by (1).

$$\theta_{th} = \frac{L}{\sigma A} \tag{1}$$

Where $\theta_{th}$ is the material thermal resistance, L is the length, $A$ is the cross-sectional area, and $\sigma$is the thermal conductivity of the material.

The transient thermal model is shown in Fig. 2(b), where each material of the structure shown in Fig. 2(a) has an associated thermal resistance and a thermal capacitance. Here, material_1, material_2, and material_5 are connected in series with a parallel combination of material_3 and material_4. In transient thermal state, the heat flows through both thermal resistance and thermal capacitance. The associated thermal capacitors are the heat capacity of the material plus a correction term due to the thermal contacts of all thermal objects [34]. Fig 2(c) shows the steady-state thermal model of the structure, where all the capacitors are fully charged and have no role in the temperature behavior of the system; therefore, they can be omitted from the thermal model, as shown in Fig. 2(c). In this model, $\Delta T$ is the temperature difference between the top side of material_1 and bottom side of material_5. The thermal resistance of the proposed model, shown in Fig. 2(c), is given by (2).

$$\theta_{th\_material} = \theta_{material\_1} + \theta_{material\_2} + \theta_{material\_3} \,//\, \theta_{material\_4} + \theta_{material\_5} \tag{2}$$

Where $\theta_{material\_1}$, $\theta_{material\_2}$, $\theta_{material\_3}$, $\theta_{material_4}$and$\theta_{material_5}$ are the thermal resistances of material_1, material_2, material_3, material_4, and

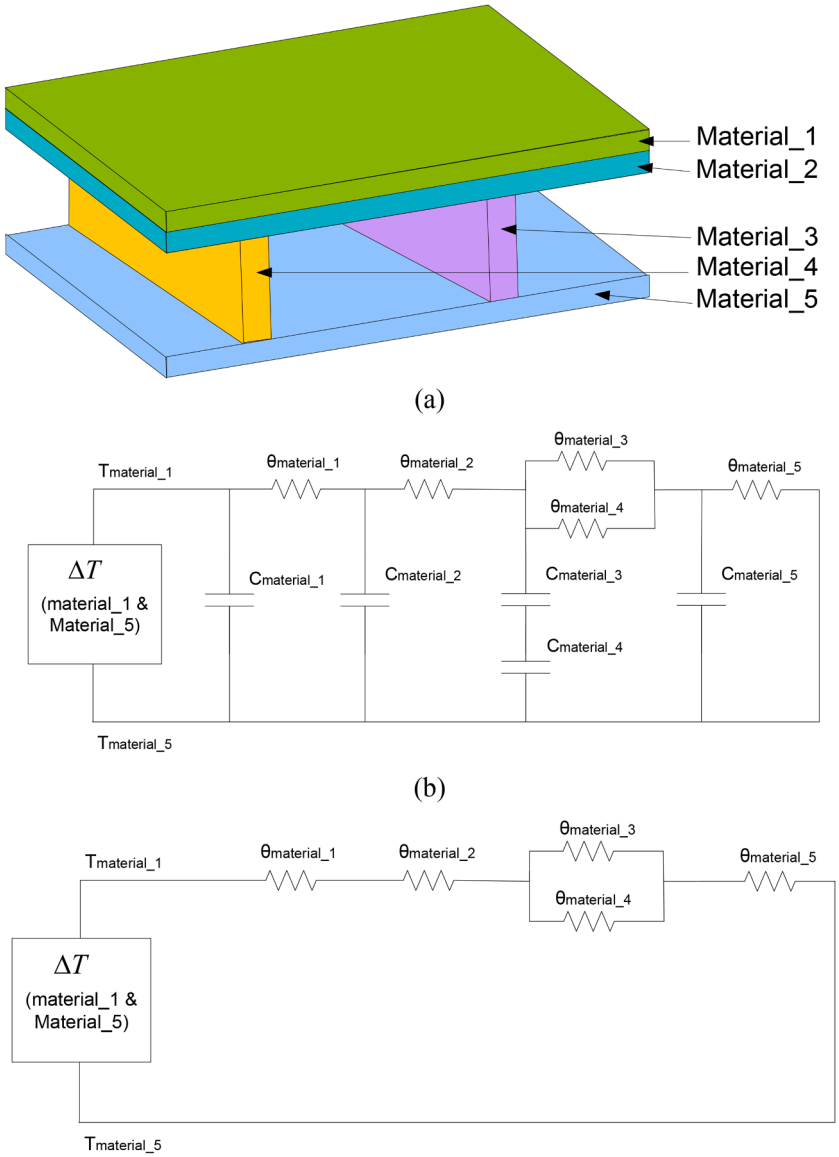


**Fig. 2.** (a) Structure composed of five materials (b) Transient thermal model (c) Steady state thermal model.

material_5, respectively, and $\theta_{th\_material}$ is the total thermal resistance of the structure from the top side of material_1 to the bottom side of material_5.

When solar radiation impinges on the top side of the structure (material_1), as shown in Fig. 2(a), it conducts to the bottom side (material_5). The temperature difference ($\Delta T$) between the illuminated face (material_1) and dark side (material_5) of the aerospace system depends on the thermal resistance ($\theta_{th\_material}$), and the incoming unwanted solar power absorbed by the structure ($P_u$) is given by (3).

$$\Delta T = P_u \cdot \theta_{th\_material} \tag{3}$$

A specific amount of incoming solar power is absorbed by the structure and a portion is reflected. The absorbed power ($P$) is given by (4).

$$P = \alpha \cdot P_d \cdot S \tag{4}$$

Where $\alpha$ is the absorptivity of the exposed surface; $P_d$ is the impinging solar power density; $S$ is the exposed surface area; and $P$ is the power absorbed by the surface.

In the case of small satellites, material_1 of the structure shown in Fig. 2(a) will have solar panels exposed to solar radiation. A fraction of percentage of the absorbed solar power is converted into useful electrical energy, whereas the remaining power is transmitted to the satellite subsystems. The power transmitted to the satellite structure accumulates as unwanted heat power. The unwanted power ($P_u$) depends on $P_d$, solar panel conversion efficiency ($\eta$), absorptivity ($\alpha$), and $S$, as given by (5).

$$P_u = P_d \cdot S \cdot (1 - \eta) \cdot \alpha \tag{5}$$

*Re*-arranging (3) and (5) yields (6).

$$\Delta T = P_d \cdot S \cdot (1 - \eta) \cdot \alpha \cdot \theta_{th} \tag{6}$$

To find $\Delta T$ for a structure as shown in Fig. 2(a), rearranging (2) and (6) will result in (7).

$$\Delta T = P_d \cdot S \cdot (1 - \eta) \cdot \alpha \cdot \left(\theta_{material\_1} + \theta_{material\_2} + \theta_{material\_3} \,/\!/\, \theta_{material\_4} + \theta_{material\_5}\right) \tag{7}$$

The Eq. (7) concludes that the temperature difference and resultant heat accumulation inside a specific structure are dependent on the impinging solar power density ($P_d$), exposed surface area ($S$), solar panel conversion efficiency ($\eta$), absorptivity ($\alpha$), and thermal resistance of the structure ($\theta_{th}$). Since all these parameters are generally fixed in the design or operational context, except the thermal resistance of the structure ($\theta_{th}$), which represents the structure's ability to resist heat transfer. A higher$\theta_{th}$ leading to low heat transfer from the illuminated face to the dark face of the satellite and greater heat buildup inside the structure. Conversely, reducing the thermal resistance allows heat to dissipate more effectively, mitigating temperature rise and heat accumulation.

Therefore, to manage heat accumulation effectively within the spacecraft structure, the focus should be on minimizing the thermal resistance. By optimizing the materials and design of the structure such as using high-conductivity materials, or designing efficient thermal pathways, the system can better handle the thermal load imposed by solar power absorption and maintain thermal stability.

## 3. Thermal models of various panels

AraMiS satellites are composed of individual panel bodies, commonly referred to as tiles, which consist of outer-facing solar panels and essential electronic components for power management, attitude determination, and inner-side control systems. These tiles vary in size and are made from different materials, such as FR4, copper, and aluminum, among others. Fig. 3 illustrates three AraMiS tiles with distinct dimensions, comprising FR4, a combination of Aluminum and FR4, and a Honeycomb structure.

### 3.1. Thermo-mechanical model of the AraMiS solar panel

The architecture of the AraMiS satellites is characterized by a configuration of six identical tiles that are strategically affixed to the external surfaces of the satellite. Among these tiles, five were specifically engineered as power management units responsible for the efficient generation and distribution of power throughout the satellite system. The sixth tile plays a pivotal role in telecommunications, accommodating essential components, such as antennas and transceivers, and facilitating seamless communication with ground stations and other spacecraft. In addition to their functional roles, these six tiles also play a critical role in providing the necessary mechanical structure to the satellite, ensuring its overall stability and structural integrity. The tiles were precisely assembled into a unified cuboid structure, with aluminum rails serving as the means of attachment, further contributing to the robustness and resilience of the satellite in a demanding space environment. To comprehensively analyze the thermal and mechanical behavior of a typical AraMiS tile, a detailed thermomechanical model is presented in Fig. 4, where *E1, E2, E3, and E4* denote the four edges of the tile, which is essential for determining its overall performance and structural characteristics. The ingenious design and integration of identical tiles forms the foundation of the AraMiS satellite, endowing it with versatility and reliability for a range of space missions.

This paper presents comprehensive generalized thermal models of an AraMiS tile, considering both the center-to-edge and edge- to-edge scenarios for a specific AraMiS panel. Using these models, the thermal resistances of the AraMiS tiles in both center-to-edge and edge-to-edge orientations were quantified. These measured resistances played a crucial role in evaluating the overall thermal resistance of the entire

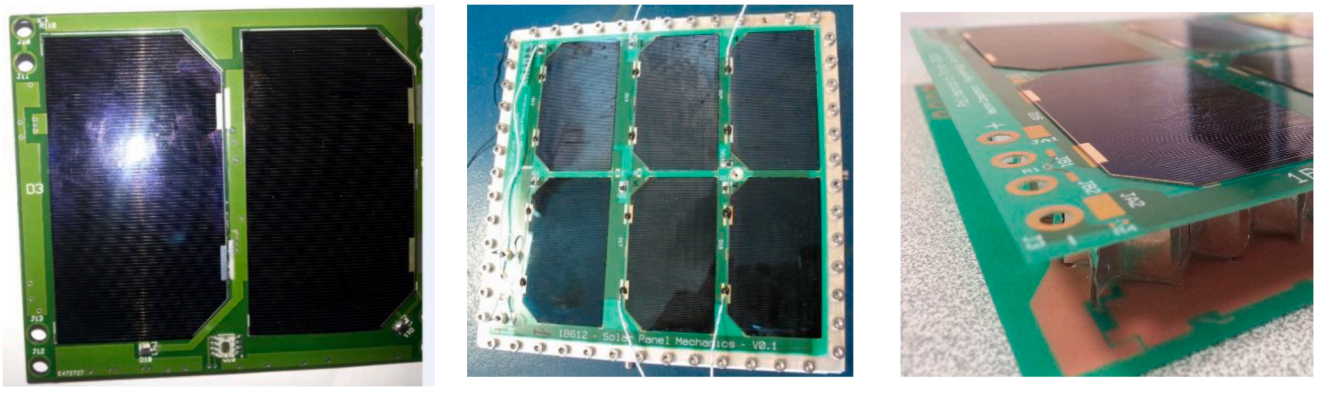


**Fig. 3.** (a) CubeSat dimension tile composed of FR4 material (b) 16.5 × 16.5cm$^2$ Aluminum structure (c) 16.5 × 16.5cm$^2$ Honeycomb structure.

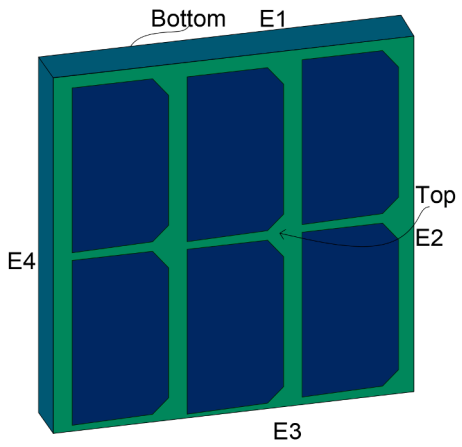


**Fig. 4.** Thermo-mechanical model of AraMiS Tile.

AraMiS satellite. It is important to note that the structural material and dimensions of the AraMiS tile may vary from one satellite to another depending on specific mission requirements. In this study, the tile was assumed to comprise a combination of solar cells, resin, aluminum, FR4, and copper materials. This analysis provides valuable insights into the thermal behavior of the AraMiS tile, contributing to the design and optimization of future satellite missions with enhanced thermal performance and reliability.

### 3.2. *Thermal model of AraMiS* $16.5 \times 16.5\ cm^2$ *tile*

AraMiS 16.5 × 16.5 $cm^2$ tile is shown in Fig. 3(b), which is composed of solar cells, resin, aluminum, copper, and FR4 materials. Apart from its intended function, the tile also acts as a mechanical structure of the AraMiS satellite. Three types of models, top-to-bottom, edge-to-edge and center-to-edge, are presented for this tile.

#### 3.2.1. *Top-to-bottom thermal model of AraMiS* $16.5 \times 16.5\ cm^2$ *tile*

The proposed thermal model presented in section-2 is applied on AraMiS 16.5 × 16.5 $cm^2$ dimension tile. Fig. 5 shows top-to-bottom cross sectional view and thermal model of the tile. This tile incorporates solar cells on its top layer and houses all the necessary electronic components related to power management, attitude determination, and control subsystems on its bottom layer (4th layer). In addition, the tile also provides a vital mechanical structure for the satellite. Furthermore, a ground plane is integrated into layers 4 and an aluminum layer 3 is added to provide extra strength to the satellite structure. The composition of this tile predominantly includes six solar cells, resins, FR4 materials, and copper materials (utilized for traces and ground planes). A cross-sectional view of the tile is presented in Fig. 5(a), where the colors green, red, pink, and blue represent the FR4 material, copper traces and ground planes, resin, and solar cells, respectively. Additionally, a corresponding thermoelectric model is provided in Fig. 5(b), where the symbols $\theta_S$,$\theta_R$, $\theta_F$, $\theta_{Al}$, and $\theta_{Cu}$represent the resistances of the solar cell, resin, FR4, aluminum and copper, respectively. The letters *'a', 'b',* and *'c'* represent the PCB various sections in Fig. 5(a) while these letters show the resistances of the corresponding sections in Fig. 5(b). Moreover, numbers 1, 2, 3, and 4 represent the resistances of the corresponding layers in Fig. 5(b). The equivalent mathematical equation of the thermal model shown in Fig. 5(b) is given in (8). The thorough examination of the tile composition and thermal-electric model presented in this paper provides valuable insights for optimizing its performance and overall thermal behavior in the AraMiS missions.

The thermal model depicted in Fig. 5(b) is expressed mathematically in (8).

$$\theta_{th\_EE} = \frac{\theta_S + \theta_R}{6} + \theta_{F\_1} + \left(\theta_{F\_a1} \Big/ \Big/ \left(\theta_{Cu\_b_2} + \theta_{F\_b_2}\right) \Big/ \Big/ \theta_{F\_c_1}\right) + \theta_{Al\_3} + \theta_{Cu\_4} + \theta_{F\_4} \tag{8}$$

#### 3.2.2. *Edge-to-Edge thermal model of AraMiS* $16.5 \times 16.5\ cm^2$ *tile*

The proposed thermal model presented in section-2 is applied on

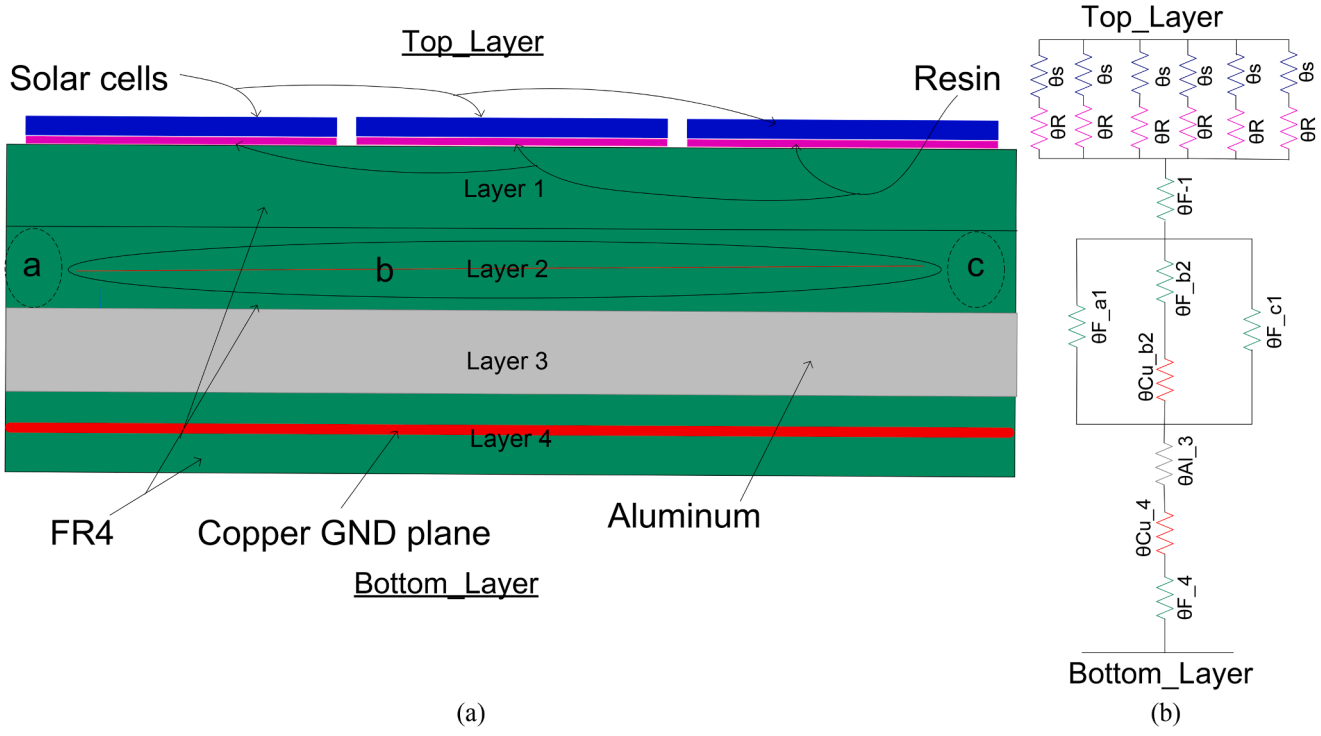


**Fig. 5.** AraMiS 16.5 × 16.5 $cm^2$ Tile (a) top-to-bottom cross-sectional view (b) thermal model.

AraMiS 16.5 × 16.5 cm$^2$ dimension tile. Fig. 6 shows top view, cross sectional view and thermal model of the tile. To determine edge-to-edge thermal resistance ($\theta_{th\_E2E4}$), the panel has been divided into small subsections (a, b, c, d, e, f, and g) of various lengths according to the type of material, as shown in Fig. 6(b). Layers 1 and 3 are entirely composed of FR4 and aluminum materials respectively, while Layers 2 and 4 are a mixture of FR4 material along with copper traces and embedded ground plane. Layers 1, 3 and 4 materials are extending in parallel from edge to edge as shown in Fig. 6(b) and therefore have corresponding thermal resistances connected in parallel as shown in Fig. 6(c). The symbols $\theta_S$,$\theta_R$,$\theta_F$,$\theta_{Cu}$,$\theta_{POS}$and $\theta_{Al}$in Fig. 6(c) represent the resistances of the solar cell, resin, FR4, copper, solar positive terminal and aluminum respectively while the letters (*'a', 'b', 'c', 'd', 'e', 'f' and* 'g') attached with these resistances symbols represent the corresponding sections resistances attached with these materials. The thermal model of Fig. 6(c) is written in mathematical form as given in (9).

$$\theta_{th\_EE} = \left(\left(\frac{3}{2}\theta_S \middle/\!/ \frac{3}{2}\theta_R \middle/\!/ \theta_{POS} \middle/\!/ \left(\theta_{Cu\_b_2} + \theta_{Cu\_c_2} + \theta_{Cu\_d_2}\right) \middle/\!/ \left(\theta_{F\_b_2} + \theta_{F\_c_2} + \theta_{F\_d_2}\right)\right) + 2\theta_{F\_e_2}\right) /\!/ \theta_{F\_f1} /\!/ \theta_{Al\_f3} /\!/ \theta_{Cu\_g4} /\!/ \theta_{F\_f4} \tag{9}$$

### 3.2.3. *Centre-to-Edge thermal model of AraMiS 16.5 × 16.5 cm$^2$ tile*

To find center-to-edge thermal model of the tile, we are dividing the tile into three concentric circles with centers $r_0$ and radii $r_1$, $r_2$ and $r_3$ as shown in Fig. 7(a). Suppose that the solar power *(E)* is striking on the center of the tile and spreads out towards the edges of the tile. The circle receiving the incoming solar power has a radius '$r_1$' and the outer circles where the power is spreading out have radii '$r_2$' and '$r_3$' as shown in Fig. 7(a). The center-to-edge thermal model is based on the thermal resistance between the two circles.

The solar power ($E$) absorbed by a circle of radius $r$ is given by (10).

$$E = \varphi\alpha\pi r^2 \tag{10}$$

Where '$\varphi$' is the solar power density and '$\alpha$' is the absorptivity of the circle surface with radius $r$.

The temperature difference ($\Delta T$) of length $dr$ is given by (11).

$$\begin{aligned} dT &= Ed\theta = E\frac{dr}{\lambda 2\pi rt} = \varphi\alpha\pi r^2\frac{dr}{\lambda 2\pi rt} = \frac{\varphi\alpha}{2\lambda t}rdr \\ \int_{r_1}^{r_2} dT &= \frac{\varphi\alpha}{2\varphi\lambda t}\int_{r_1}^{r_2} rdr = \frac{\alpha\left(r_2^2 - r_1^2\right)}{4\lambda t} \\ \Delta T &= \frac{\alpha\varphi}{4\lambda t}\left(r_2^2 - r_1^2\right) \end{aligned} \tag{11}$$

Here '$\lambda$' is the thermal conductivity of the material and '$t$' is the thickness of the circular section.

The thermal resistance of a section with length $dr$, as shown in Fig. 8, is given by (12).

$$\Delta\theta = \frac{\Delta T}{E} = \frac{\frac{\alpha\varphi r^2}{4\lambda t}}{\varphi\cdot\pi\cdot r^2} = \frac{\alpha}{4\pi\lambda t} \tag{12}$$

The above equation shows that thermal resistance of a circular section depends on the thickness '$t$' and the material absorptivity *($\alpha$)*.

In Fig. 7(b), the circle with radius $r_1$ contains the FR4 material and the ground plane (extended in layer 4). The subsection between circles $r_1$ and $r_2$ contains copper traces, FR4 material, and ground plane. The subsection between circles $r_2$ and $r_3$ contains the FR4 material and ground plane. The center-to-edge thermal model ($\theta_{th\_CE}$) is shown in Fig. 7(c). Here, $r_ir_j$ $(i, j = 0, 1, 2, 3)$ represents the subsections of the three

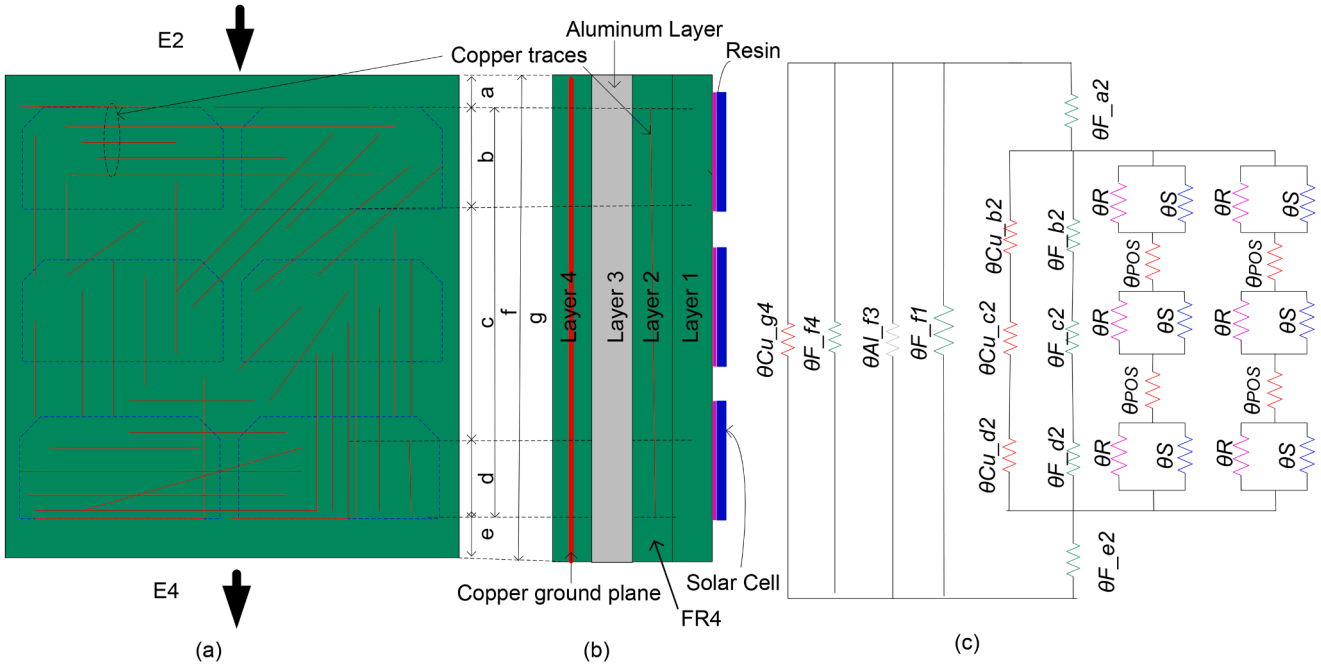


**Fig. 6.** AraMiS Tile (a) top view (b) cross-sectional side view (c) thermal model.

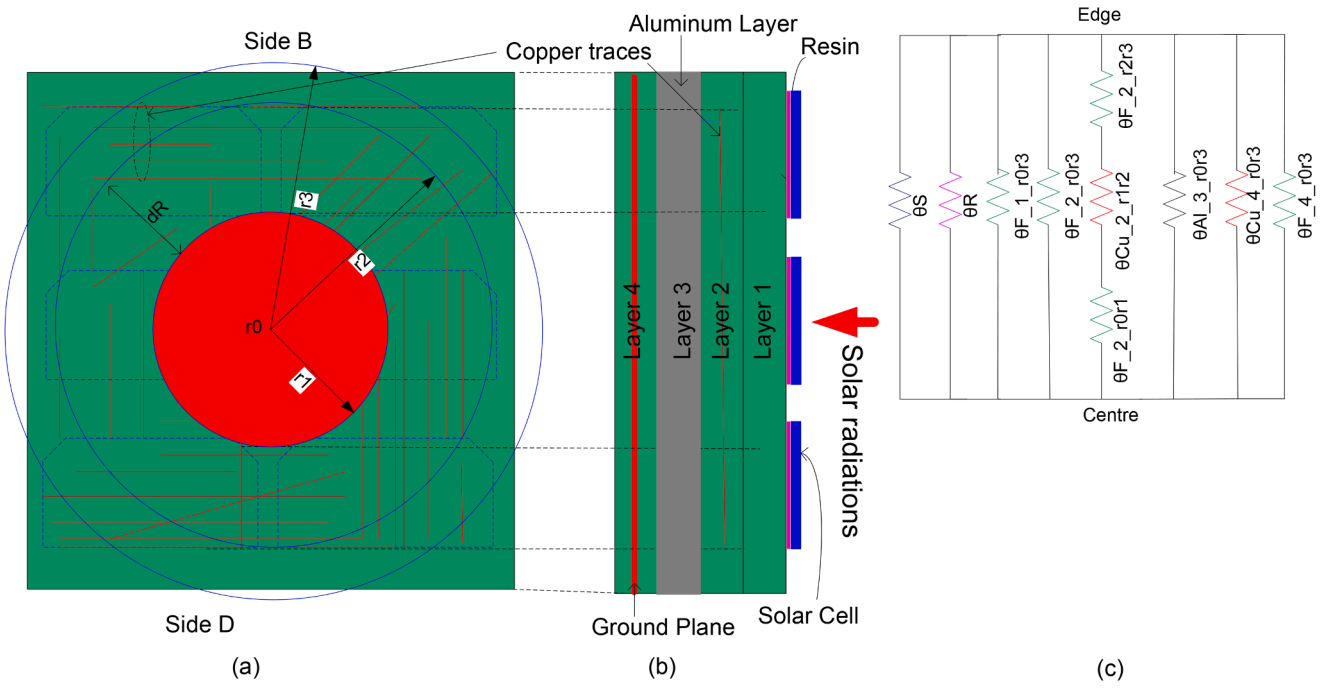


**Fig. 7.** Tile (a) Top view (b) cross-sectional view (c) thermal model.

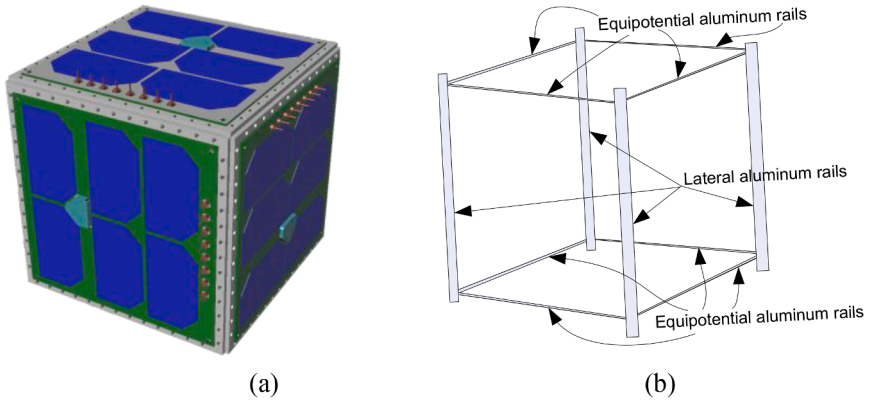


**Fig. 8.** AraMiS 16.5 × 16.5 × 16.5cm$^3$ satellite (a) actual satellite (b) structure frame.

circles. For example, $\theta_{F\_2\_r2r3}$ represents the thermal resistance of the FR4 material in layer 2 of the subsection between the circles $r_2$ and $r_3$. The rest of the modeling representation is identical to that of the previous models.

The thermal model of Fig. 7(c) is written in mathematical form as given in (13).

$$\theta_{th\_CE} = \theta_S // \theta_R // \theta_{F\_1\_r_0r_3} // \theta_{F\_2\_r_0r_3} // (\theta_{F\_2\_r_0r_1} + \theta_{Cu\_2\_r_1r_2} + \theta_{F\_2\_r_2r_3}) // \theta_{Al\_3\_r_0r_3} // \theta_{Cu\_4\_r_0r_3} // \theta_{F\_4\_r_0r_3} \quad (13)$$

## 4. Thermal model of the AraMiS cubic satellite

In the thermal model of the AraMiS satellites, we analytically measured the thermal resistances of various dimensions of AraMiS satellites, that is, 1 U (16.5 × 16.5 × 16.5 cm$^3$), 4 U (33 × 16.5 × 33 cm$^3$) and 8 U (33 × 33 × 33 cm$^3$), as shown in Figs. 8(a), 11(a), and 14(a), respectively. These thermal resistances are measured from the center of the tile exposed to solar radiation to the center of the tile mounted on the dark side (i.e., opposite face to incoming solar radiation). The AraMiS satellite is composed of six tiles mounted on the external periphery of the satellite. These tiles are connected by satellite structures composed of aluminum rails (as shown in Figs. 8(b), 11(b), and 14(b), respectively). The AraMiS 16.5 × 16.5 cm$^2$ satellite structure is composed of twelve aluminum rails connected together and six tiles mounted on these rails, as shown in Fig. 8. Tiles and aluminum rails have associated thermal resistances.

To measure the thermal resistance of a specific satellite, we assumed that incoming solar radiation is perceived by the center of the illuminated tile with the highest temperature. It then flows through the lateral tiles and aluminum rails (mounted on the four lateral faces) towards the dark side (i.e., the minimum temperature point) of the satellite, which is mounted on the opposite face of the illuminated tile. The illuminated tile will have center-to-edge thermal resistance ($\theta_{th\_CE}$), while the four lateral tiles will have four parallel edge-to-edge thermal resistances ($\theta_{th\_EE}$) along with the lateral aluminum rails of the structure frame. The heat finally flows to the center of the dark face tile with center-to-edge thermal resistance ($\theta_{th\_CE}$).

### 4.1. *Thermal model of AraMiS 1U cubic satellite*

Eventually, we are ready to employ the proposed thermal model on the AraMiS satellites to measure their thermal resistance. In the case of

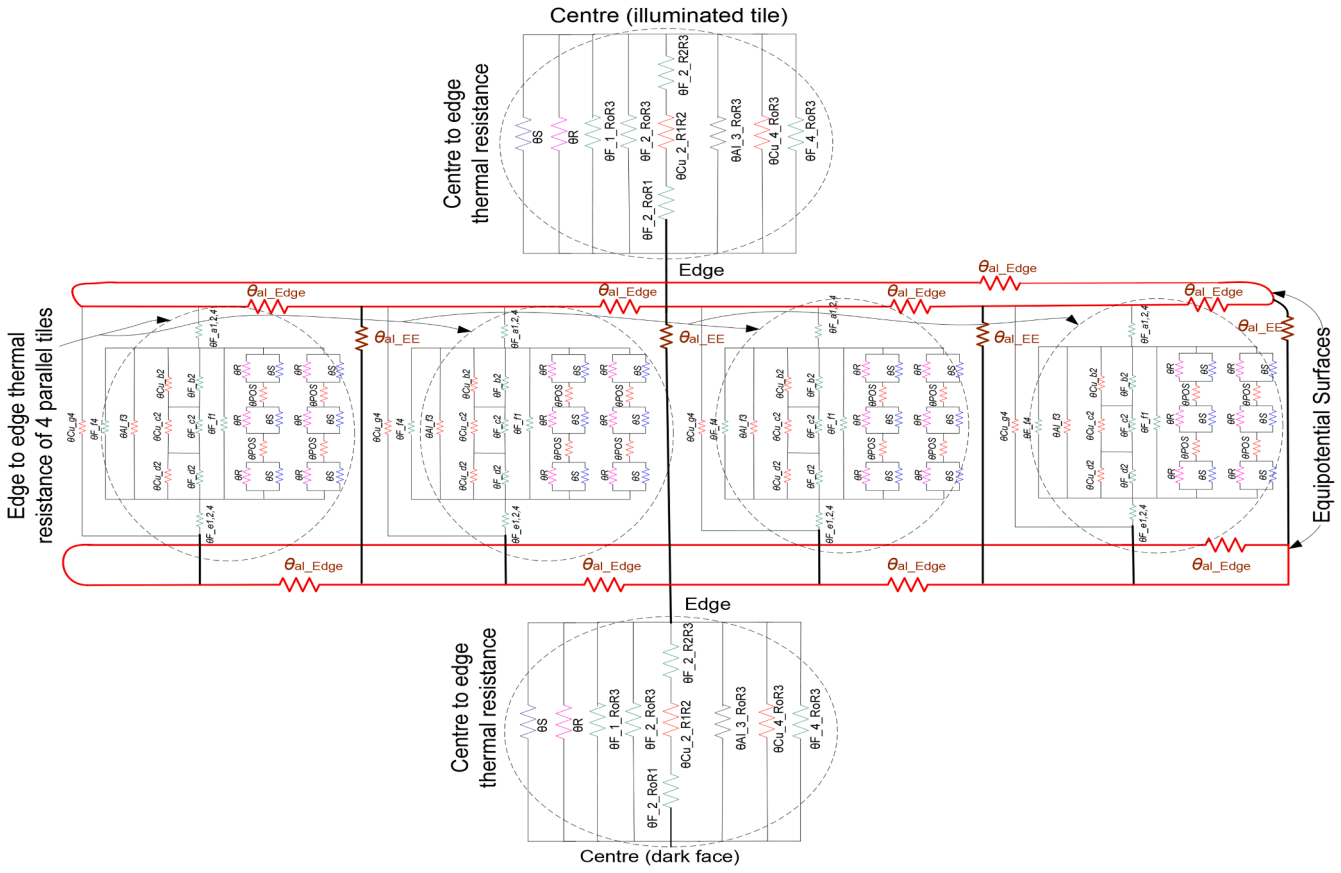


**Fig. 9.** AraMiS 16.5 × 16.5 × 16.5cm$^3$ satellite detailed thermal model.

the AraMiS 1 U satellite, there is one illuminated tile, four lateral tiles, and a single tile on the dark face. The detailed thermal model of the AraMiS 1 U satellite is shown in Fig. 9, where the illuminated tile has center-to-edge thermal resistance ($\theta_{th\_CE}$), and the four lateral tiles have associated edge-to-edge thermal resistances ($\theta_{th\_EE}$). The satellite tile mounted on the dark face has an associated center-to-edge thermal resistance ($\theta_{th\_CE}$). The models of the thermal resistances $\theta_{th\_CE}$ and $\theta_{th\_EE}$ shown in Fig. 9 are inserted from the thermal models of the AraMiS tiles shown in Figs. 6 and Fig. 7 respectively. Four aluminum rail thermal resistances ($\theta_{al\_EE}$) associated with the aluminum rails of the satellite frame structure are connected in parallel with $\theta_{th\_EE}$, further reducing the overall satellite thermal resistance and are integral parts of the satellite thermal model. Eight aluminum thermal resistances ($\theta_{al\_Equ}$) are connected on the two equipotential surfaces as shown in Fig. 9. The surfaces of the satellite thermal model at the same temperature level are termed as equipotential surfaces. No net heat flow across the equipotential surfaces, therefore $\theta_{al\_Equ}$ resistances play no role in the satellite equivalent thermal resistance and can be omitted from the satellite thermal model. The complete thermal model of the satellite is shown in Fig. 9, where each tile and satellite aluminum frame has all the respective associated thermal resistances. The nomenclature used for the thermal resistance representation shown in the AraMiS complete thermal model in Fig. 9 is already provided in the respective tile thermal models discussed in Sections 3.1 and 3.2. Here, the new resistances are the satellite structure aluminum rail thermal resistances $\theta_{al\_Equ}$ and $\theta_{al\_EE}$. Consequently, there are four $\theta_{th\_EE}$ and four $\theta_{al\_EE}$ connected in parallel to attach the illuminated tile on one end with the dark tile on the other side. A simplified thermal model of the complete satellite is shown in Fig. 10, where each tile is represented by a single thermal resistance. Here, the complete satellite thermal model is reduced to two $\theta_{th\_CE}$, four $\theta_{th\_EE}$, and four $\theta_{al\_EE}$ values. The AraMiS 1 U satellite thermal model shown in Fig. 10 can be expressed mathematically, as given in (14).

$$\theta_{th\_sat\_1U} = 2\theta_{th\_CE} + \left(\frac{\theta_{th\_EE}}{4} \Big/\!\Big/ \frac{\theta_{al\_EE}}{4}\right) \tag{14}$$

Calculated values of the AraMiS 1 U satellite and its tile resistances in various directions are given in Table 1.

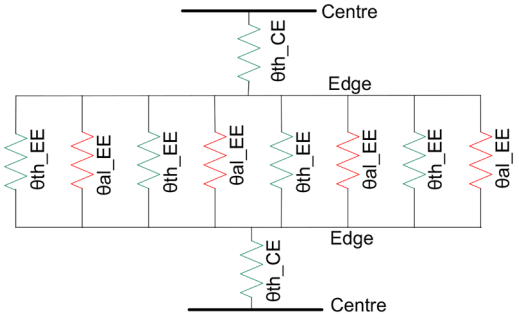


**Fig. 10.** AraMiS 16.5 × 16.5 × 16.5cm$^3$ satellite simplified thermal model.

### 4.2. *Thermal model of AraMiS 4U cubic satellite*

In the case of AraMiS 4 U satellite, there are 4 illuminated tiles, 8 lateral tiles, 8 lateral aluminum rails and 4 tiles on the dark face. The detailed thermal model of the AraMiS 4 U satellite is shown in Fig. 12, where the illuminated tiles have four parallel centre-to-edge thermal resistances ($\theta_{th\_CE}$) and the lateral tiles have eight parallel associated edge-to-edge thermal resistances ($\theta_{th\_EE}$). The tiles mounted on the dark face have four parallel associated centre-to-edge thermal resistances ($\theta_{th\_CE}$). The models of the thermal resistances $\theta_{th\_CE}$ and $\theta_{th\_EE}$ shown in

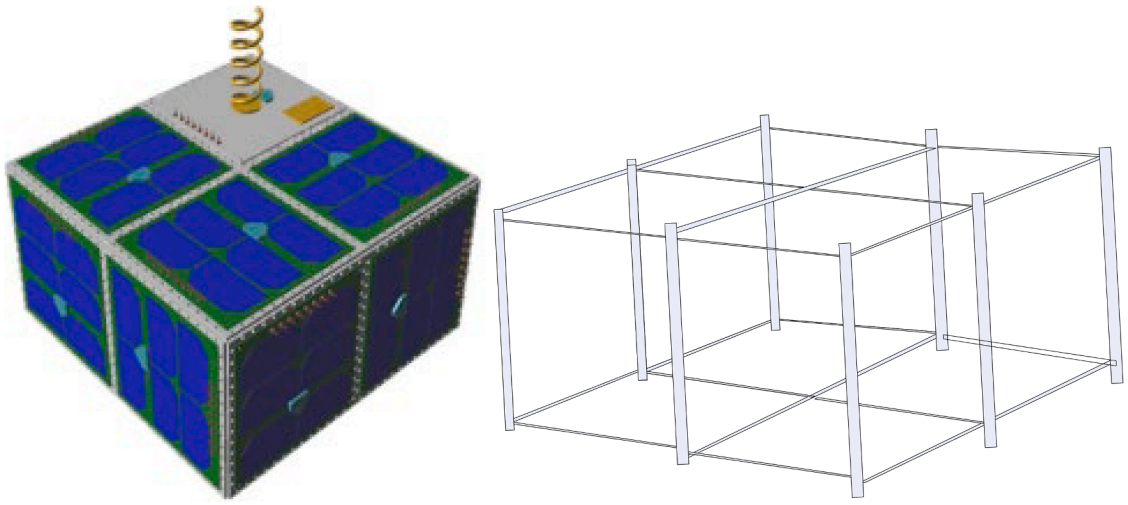

(a) (b)

**Fig. 11.** AraMiS 4 U satellite (a) actual satellite (b) structure frame.

**Table 1**
Calculated thermal resistances of AraMiS 1 U (16.5 × 16.5 × 16.5cm$^3$) satellite.

| Thermal Resistance | Symbol | Value |
|---|---|---|
| center-to-edge | $\theta_{th\_CE}$ | $0.86^oC/W$ |
| edge-to-edge | $\theta_{th\_EE}$ | $1.66^oC/W$ |
| aluminum rail | $\theta_{al\_EE}$ | $0.046^oC/W$ |
| AraMiS 1 U Satellite thermal resistance | $\theta_{th\_sat\_1U}$ | $1.73^oC/W$ |

Fig. 12 are inserted from the thermal models of the AraMiS tiles shown in Figs. 6 and Fig. 7, respectively. Eight aluminum rail thermal resistances ($\theta_{al\_EE}$) which are associated with the aluminum rails of the satellite frame structure are connected in parallel with $\theta_{th\_EE}$. Sixteen aluminum thermal resistances ($\theta_{al\_Equ}$) are connected on the two equipotential surfaces (eight on each surface) as shown in Fig. 12. The $\theta_{al\_Equ}$ resistances play no role in the satellite equivalent thermal resistance and can be neglected. The complete thermal model of the satellite is given in Fig. 12 while the simplified thermal model of the complete satellite is given in Fig. 13, where each tile is represented with a single thermal resistance. Here, the complete satellite thermal model reduces to 8 $\theta_{th\_CE}$, 8 $\theta_{th\_EE}$ and 8 $\theta_{al\_EE}$. The AraMiS 4 U satellite thermal model given in Fig. 13 can be expressed mathematically as given in (15).

$$\theta_{th\_sat\_4U} = \frac{\theta_{th\_CE}}{2} + \left(\frac{\theta_{th\_EE}}{8} \Big/\Big/ \frac{\theta_{al\_EE}}{8}\right) \tag{15}$$

Calculated values of the AraMiS 4 U satellite and its tile resistances in various directions are given in Table 2. The table shows that $\theta_{th\_CE}$, $\theta_{th\_EE}$ and $\theta_{al\_EE}$ are same for 1 U and AraMiS 4 U satellites because 4 U is a modular replica of 1 U satellite. The overall thermal resistance for AraMiS 4 U satellite ($\theta_{th\_sat\_4U}$) has decreased 4 times because 4 modular 1 U satellites are connected in parallel in the 4 U structure.

### 4.3. *Thermal model of AraMiS 8U cubic satellite*

In the case of AraMiS 8 U satellite, there are 16 lateral tiles, 4 illuminated tiles facing solar radiations and 4 dark tiles mounted on the dark face of the satellite. The sixteen lateral tiles are divided into two series connected banks of lateral tiles and aluminum rails. Each bank is

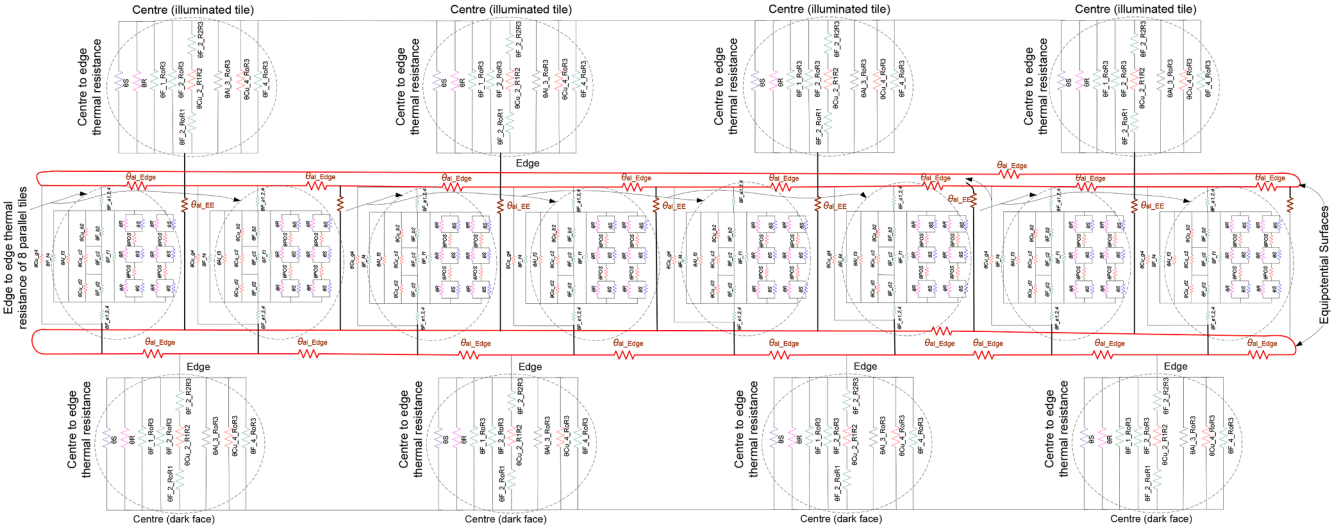


**Fig. 12.** AraMiS 33 × 16.5 × 33 cm$^3$ satellite detailed thermal model.

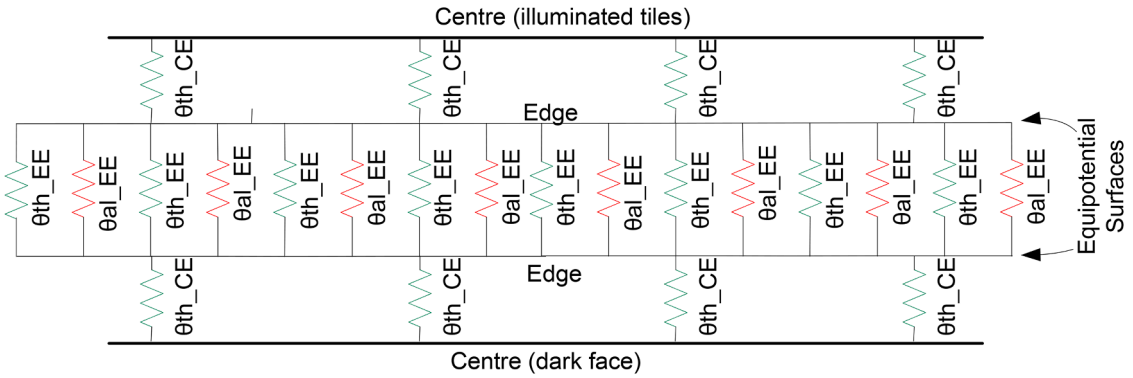


**Fig. 13.** AraMiS 33 × 16.5 × 33 $cm^3$ satellite simplified thermal model.

**Table 2**
Calculated thermal resistances of AraMiS 4 U satellite.

| Thermal Resistance | Symbol | Value |
|---|---|---|
| center-to-edge | $\theta_{th\_CE}$ | $0.86°C/W$ |
| edge-to-edge | $\theta_{th\_EE}$ | $1.66°C/W$ |
| aluminum rail | $\theta_{al\_EE}$ | $0.046°C/W$ |
| AraMiS 4 U Satellite thermal resistance | $\theta_{th\_sat\_4U}$ | $0.435°C/W$ |

similar to the 4 U lateral structure (i.e., consisted of 8 lateral tiles and 8 lateral aluminum rails) as shown in Fig. 14. The corresponding detailed thermal model of the AraMiS 8 U satellite is shown in Fig. 15, where the illuminated tiles have four parallel centre-to-edge thermal resistances ($\theta_{th\_CE}$) and the dark face have four associated parallel connected centre-to-edge thermal resistances ($\theta_{th\_CE}$). The 16 lateral tiles divided into two series connected banks have the same number of associated edge-to-edge thermal resistances ($\theta_{th\_EE}$) and the satellite frame structure has 16 aluminum rail thermal resistances ($\theta_{al\_EE}$). Each bank is similar to the 4 U satellite lateral structure where 8 $\theta_{th\_CE}$ and 8 $\theta_{al\_EE}$ are connected in parallel. Twenty-four aluminum thermal resistances ($\theta_{al\_Equ}$) are connected on the three equipotential surfaces (eight on each surface) as shown in Fig. 15. The $\theta_{al\_Equ}$ resistances play no role in the satellite equivalent thermal resistance and can be neglected. The models of the thermal resistances $\theta_{th\_CE}$ and $\theta_{th\_EE}$ shown in Fig. 15 are inserted from the thermal models of the AraMiS tiles given in Figs. 6 and Fig. 7, respectively. The complete thermal model of the satellite is given in Fig. 15 while the simplified thermal model of the complete satellite is given in Fig. 16, where each tile is represented with a single thermal resistance. Here, the complete satellite thermal model reduces to 8 $\theta_{th\_CE}$, 16 $\theta_{th\_EE}$ and 16 $\theta_{al\_EE}$. The AraMiS 8 U satellite thermal model given in Fig. 15 can be expressed mathematically as given in (16).

$$\theta_{th\_sat\_8U} = \frac{\theta_{th\_CE}}{2} + \left(\frac{\theta_{th\_EE}}{4} \Big/\Big/ \frac{\theta_{al\_EE}}{4}\right) \tag{16}$$

Thermal resistance value of the AraMiS 8 U satellite ($\theta_{th\_sat\_8\ U}$) using (14) and Table 1 is 0.441 °C/W. The thermal resistance of AraMiS 8 U satellite is a bit more than the AraMiS 4 U structure because of the one extra series connected lateral bank.

## 5. AraMiS thermal resistance practical measurement

In the preceding part of the paper, a thermal model was presented for the AraMiS satellite, and theoretical values of the thermal resistances of the AraMiS tiles and complete satellites were determined. To verify the theoretical values, the practical thermal resistance was measured using the experimental setup shown in Fig. 17(a) and (b). The laboratory setup consisted of a vacuum chamber, data acquisition system, temperature sensors, and the system under test (AraMiS satellite and tiles).

To measure the thermal resistance of the AraMiS satellite, a source is required to provide thermal power to the satellite that is equivalent to the solar radiation at AM0 (e.g., solar power at AM0 is 1366 $W/m^2$). Solar simulators can be used to provide AM0 equivalent solar radiation, but here, we are going to perform this measurement inside a vacuum chamber, and it is not possible to place a solar simulator inside a small vacuum chamber. For this purpose, a 2.2 Ω/100 W power resistor is used, which increases the satellite single-face temperature up to the temperature increase by AM0 sunlight. One of the AraMiS tile (16.5 × 16.5 $cm^2$) which harvests solar power and also provides basic structure to the AraMiS 1 U (16.5 × 16.5 × 16.5 $cm^3$), AraMiS 4 U (33 × 16.5 × 33 $cm^3$) and AraMiS 8 U (33 × 33 × 33 $cm^3$) satellites is used in the thermal

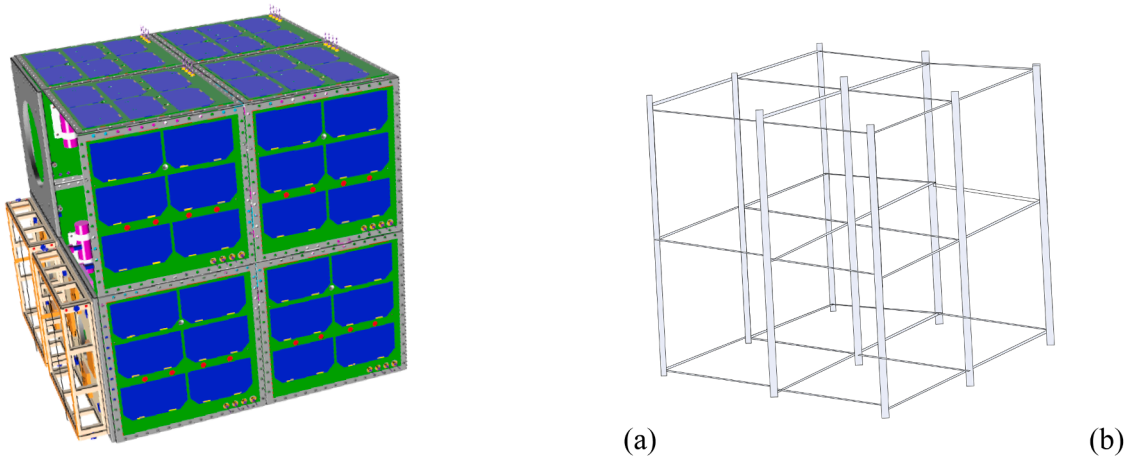


**Fig. 14.** AraMiS 33 × 33 × 3 3$cm^3$ satellite (a) actual satellite (b) structure frame.

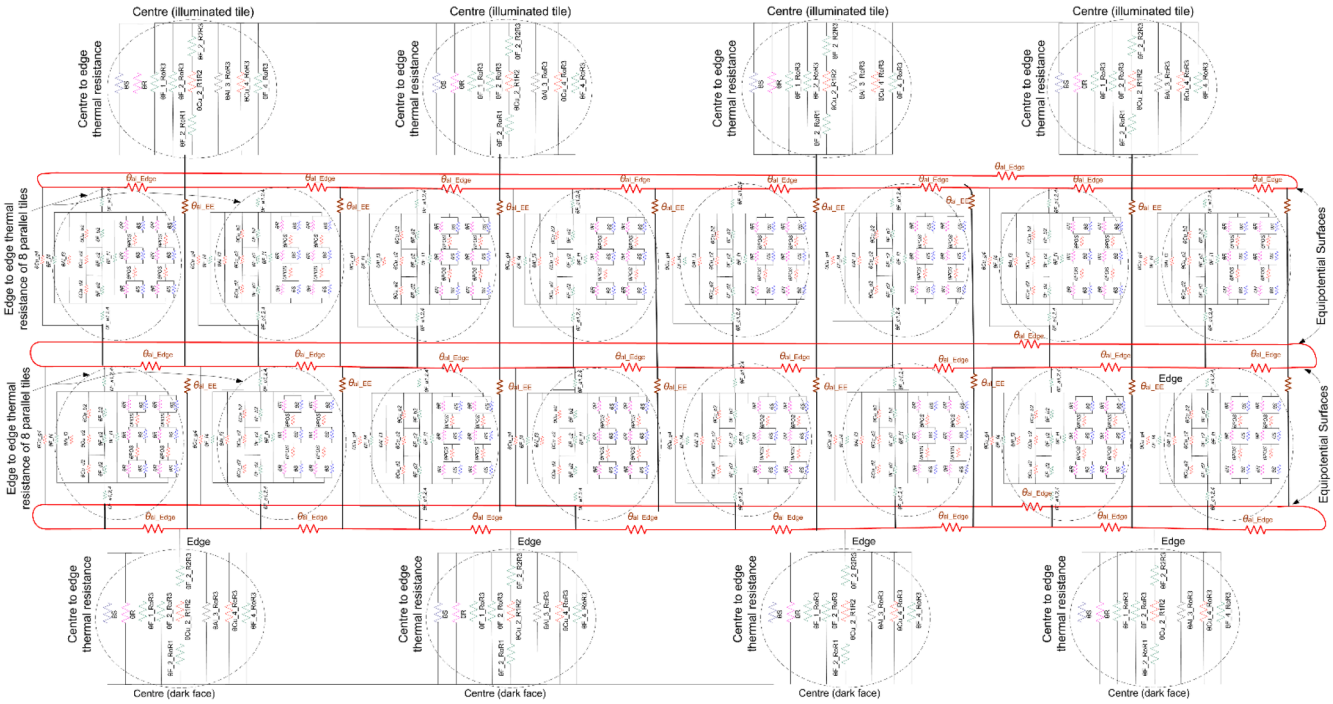


**Fig. 15.** AraMiS 33 × 33 × 33 $cm^3$ satellite detailed thermal model.

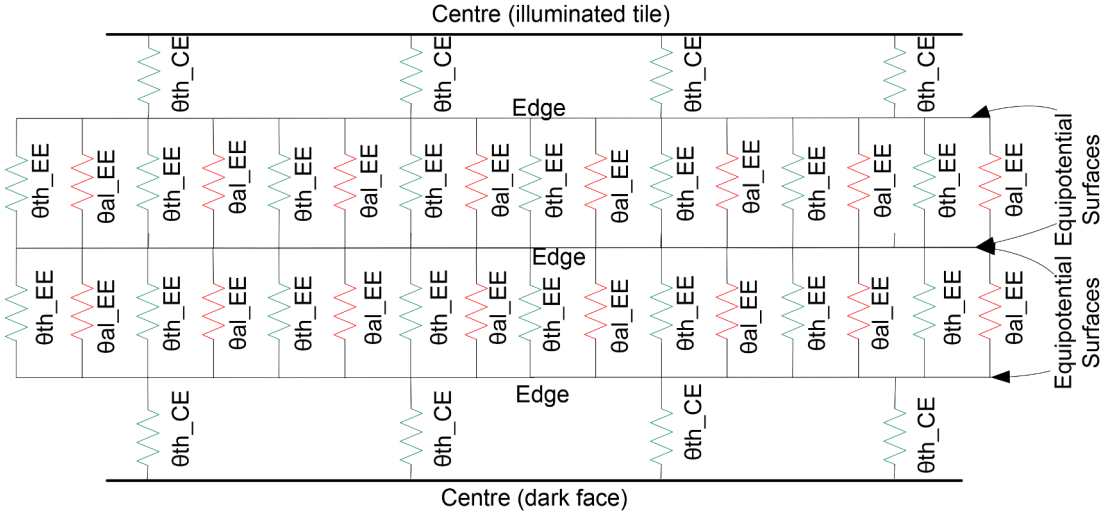


**Fig. 16.** AraMiS 33 × 33 × 33 $cm^3$ satellite simplified thermal model.

measurement as shown in Fig. 17(a).

To measure the thermal resistance of a tile, the power absorbed by the system and the corresponding temperature difference values are required, as expressed in (3). In the thermal measurement setup, an AraMiS satellite was placed inside the vacuum chamber, and a vacuum was generated in the chamber through a vacuum pump. Power equivalent to solar power is provided to the satellite through a 2.2 Ω/100 W power resistor. The AraMiS 1 U satellite, with a cubic shape and tile dimensions of 16.5 × 16.5 $cm^2$ (0.027 $m^2$), has one, two or at most three panels exposed to sunlight at a time. When a single panel is exposed to solar radiation at AM0 (1366 W/$m^2$), it absorbs 37.2 W of power (1366 W/$m^2$ × 0.027 $m^2$). If two panels are exposed at a 45° angle to the sunlight, the total equivalent panel surface area, accounting for their size and inclination, is approximately 0.038 $m^2$ (0.027 × cos (45°) × 2). Under these conditions, the absorbed solar power is about 51.9 W. If three panels are exposed to sunlight, the sunlight will strike the panels at different angles due to the geometry of the AraMiS 1 U cubic shape. Assuming the cube's edges are aligned with a Cartesian coordinate system, and sunlight is coming from a direction perpendicular to one of the cube's diagonals, then the angle of incidence for each panel will be 54.74° and the effective surface area will be 0.047 $m^2$ (0.027 × cos (54.74°) × 3). The absorbed solar power will be 63.87 W (1366 W/$m^2$ × 0.027 $m^2$).

To validate the thermal resistance measured through our proposed model for the AraMiS satellite and its tiles, here we are going to measure its values through an experimental setup. As single tile is absorbing 37.2 W power when exposed to solar radiations at AM0, therefore, we must provide a power of 37.2 W to the AraMiS satellite on one tile, assuming that it is the top tile facing solar radiation. To provide 37.2 W of power to the AraMiS satellite, a constant current of 4.1A was drawn through a 2.2 Ω/100 W power resistor. Three temperature sensors are used to measure the temperature difference between top, bottom and lateral tiles of the

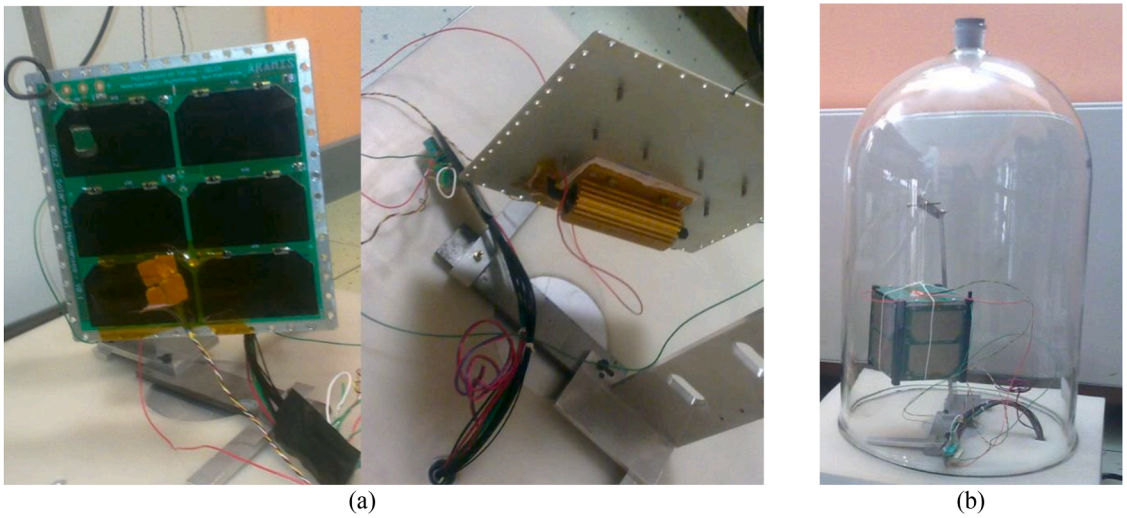


**Fig. 17.** (a)Solar panel with power resistor and temperature sensor (b) Vacuum chamber with one of the AraMiS satellite.

satellite. One temperature sensor is attached to the illuminated tile with a 2.2 Ω/100 W power resistor, 2nd temperature sensor is attached to the lateral side tile and a 3rd temperature sensor is attached to the dark tile (i.e., opposite face of the power resistor tile). The illuminated and dark side temperature sensors measured the temperature difference between top and bottom side tiles of the satellite. Temperature sensor data were acquired using a data acquisition system. When 37.2 W of power is applied through the power resistor, the illuminated tile started heating, and the heat flew towards the dark tile through lateral tiles. The temperature sensor values started to increase. After some time, the temperature of the tiles attained steady-state values and the data from the temperature sensors became stable. All the sensor data were acquired and recorded continuously during the experiment.

The thermal resistance of the AraMiS-U1 satellite was experimentally measured using the setup depicted in Fig. 17, and the results are presented in Fig. 18. The duration of these measurements was 133 mins. Notably, the temperature of the top tile increased upon the application of heat (37.2 W) through a power resistor. This thermal energy propagates to both the lateral and bottom tiles, causing a corresponding increase in their temperatures. After approximately 80 min, the system reached a state of thermal equilibrium, as is evident from the plots where no further increase in the temperatures of the respective tiles was observed. The thermal resistance, determined through the experimental setup, was found to be 1.83 $^{\circ}C/W$ (91.76 × 0.02). This value closely aligns with the theoretically predicted thermal resistance of 1.73 $^{\circ}C/W$, as derived from our proposed model given in Table 1.

Here in the above experimental thermal resistance measurement, we haven't assumed the terrestrial albedo's reflected radiation effect. Terrestrial albedo plays a significant role in the thermal analysis of spacecraft [35,36]. It represents the proportion of sunlight reflected from the Earth's surface back into the atmosphere without being absorbed. This value varies across the Earth's surface, influenced by

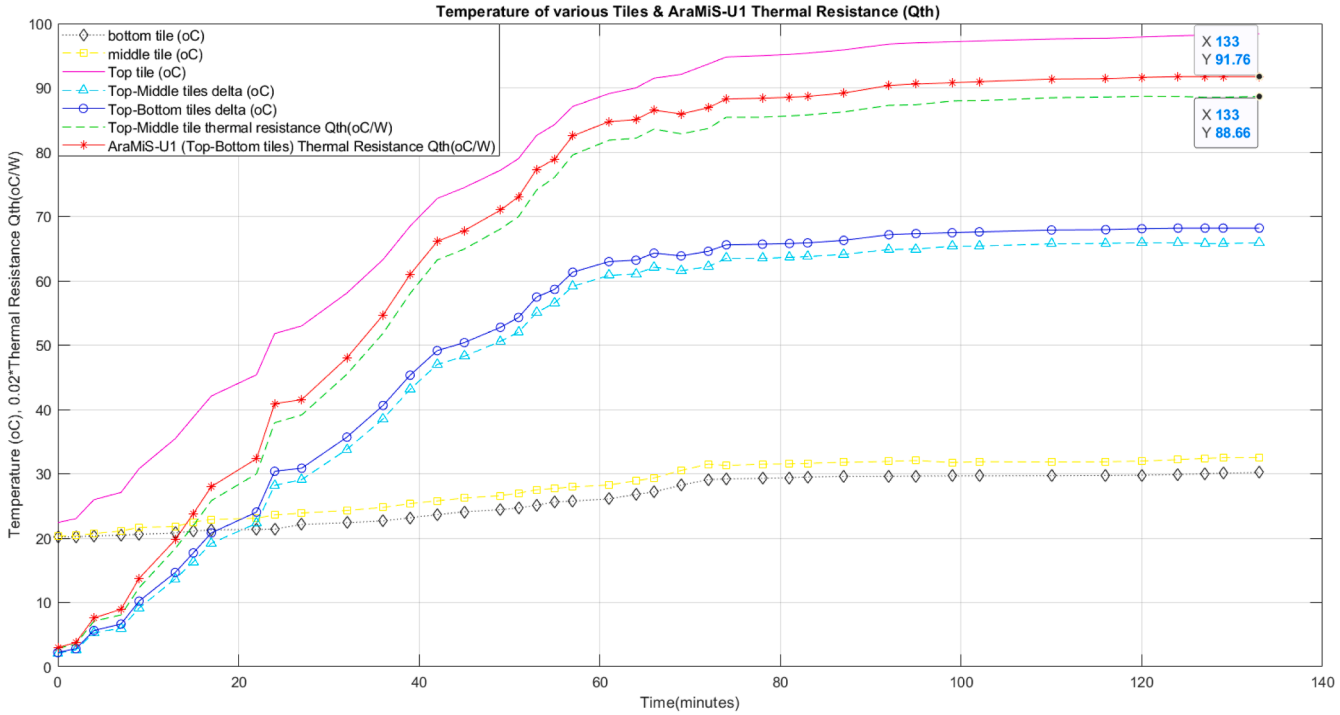


**Fig. 18.** Practically measured thermal resistances ($Q_{th}$) values of AraMiS-1 U satellite.

factors such as regional atmospheric conditions and surface characteristics, including snow, forests, deserts, and oceans. On average, terrestrial albedo is slightly below then 0.4 [35,36].

For the AraMiS system, which orbits relatively close to the Earth's surface (<1/5th of the Earth's radius), the Earth's reflected radiation can be approximated as the product of solar radiation and Earth's albedo, which yields $1366 \times 0.4 = 546\ W/m^2$. However, at an altitude of 1200 km, this value decreases by approximately 70 % [37,38], which results in a received power of $546 \times 0.3 = 163\ W/m^2$ and the AraMiS 1 U with dimension 0.027 $m^2$ will receive $163 \times 0.027 = 4$ W.

Thermal resistance ($\theta_{th} = \Delta T/P$) is defined as the ratio of the temperature difference ($\Delta T$) to the power flow ($P$) through a structure. If the effect of Earth's albedo-reflected radiation is neglected, will result in higher $\Delta T$, leading proportionally to a higher power flow ($P$). However, the thermal resistance ($\theta_{th}$, ratio between $\Delta T$ and $P$) will remain constant for a given structure, as it is a property determined by the material and geometry of the structure.

## 6. Conclusion

In this paper, a preliminary thermal model is presented for the AraMiS multicube small spacecraft. The proposed model is composed of thermal resistors and thermal capacitors; however, in the case of thermal equilibrium, the capacitors are fully charged and do not contribute to heat flow. Therefore, the final model was reduced to thermal resistors. The anticipated model is applied to the AraMiS 16.5 × 16.5 $cm^2$ dimension tile and the corresponding thermal resistance network, and the equivalent mathematical modeling equation is derived. In the mathematical model of the AraMiS 16.5 × 16.5 $cm^2$ dimension tile, each material, that is, FR4, copper, aluminum, etc., has its own corresponding thermal resistance, whose value is dependent on the dimensions of the respective material. the AraMiS 16.5 × 16.5 $cm^2$ dimension tile resistor in the thermal models of AraMiS-1 U the AraMiS-4 U and AraMiS-8 U satellites, and the AraMiS 16.5 × 16.5 $cm^2$ is represented by a single resistor in the thermal models of the AraMiS multiunit satellites. The thermal resistances of the AraMiS 16.5 × 16.5 $cm^2$ tile and the AraMiS-1 U satellite are measured through an experimental setup.

The theoretical values measured using the proposed model had very small deviations from the experimental results, which demonstrates the accuracy of the proposed model. The proposed model can be applied to a small spacecraft to measure the thermal resistance of the structure. The thermal resistance values of the AraMiS multi-cube structures measured using this model are very low, indicating that the heat absorbed by the satellite-illuminated face can be easily dissipated to the cooler dark face.

The proposed model serves as an effective tool during the initial spacecraft design phase. It allows researchers and engineers to find suitable materials and dimensions necessary to achieve a targeted thermal resistance for the spacecraft structure. Researchers can experiment with various material types and dimensions to achieve their desired thermal resistance values.

## CRediT authorship contribution statement

**Anwar Ali:** Writing – original draft, Resources, Methodology, Investigation, Formal analysis, Conceptualization. **Muhammad Rizwan Mughal:** Visualization, Validation, Methodology, Formal analysis. **Shoaib Ahmed Khan:** Writing – original draft, Methodology, Formal analysis. **Kar Seng Teng:** Writing – original draft, Resources.

## Declaration of competing interest

On behalf of all authors, the corresponding author declares here that there is no conflict of interest concerning the publication of this article.

## Data availability

No data was used for the research described in the article.

## References


[1] N. Frischauf, R. Horn, T. Kauerhoff, M. Wittig, I. Baumann, E. Pellander, O. Koudelka, NewSpace: New Business Models at the Interface of Space and Digital Economy: Chances in an Interconnected World, New Space, 2018.

[2] G. Peters, Utilizing commercial best practices for success in NewSpace, Microw. J. (2015).

[3] S. Carletta, M. Pontani, P. Teofilatto, An Earth-Mars microsatellite mission leveraging low-energy capture and low-thrust propulsion, Acta Astronaut. 200 (2022) 635–646, https://doi.org/10.1016/j.actaastro.2022.09.034. ISSN 0094-5765.

[4] J. Praks, M. Rizwan Mughal, R. Vainio, P. Janhunen, J. Envall, P. Oleynik, A. Näsilä, H. Leppinen, P. Niemelä, A. Slavinskis, J. Gieseler, P. Toivanen, T. Tikka, T. Peltola, A. Bosser, G. Schwarzkopf, N. Jovanovic, B. Riwanto, A. Kestilä, A. Punkkinen, R. Punkkinen, H.-P. Hedman, T. Säntti, J.-O. Lill, J.M.K. Slotte, H. Kettunen, A. Virtanen, Aalto-1, multi-payload CubeSat: design, integration and launch, Acta Astronaut. 187 (2021) 370–383, https://doi.org/10.1016/j.actaastro.2020.11.042. ISSN 0094-5765.

[5] M.R. Mughal, J. Praks, R. Vainio, P. Janhunen, J. Envall, A. Näsilä, P. Oleynik, P. Niemelä, A. Slavinskis, J. Gieseler, N. Jovanovic, B. Riwanto, P. Toivanen, H. Leppinen, T. Tikka, A. Punkkinen, R. Punkkinen, H.-P. Hedman, J.-O. Lill, J.M. K. Slotte, Aalto-1, multi-payload CubeSat: in-orbit results and lessons learned, Acta Astronaut. (2021), https://doi.org/10.1016/j.actaastro.2020.11.044. ISSN 0094-5765.

[6] D.J. Robson, C. Cappelletti, Biomedical payloads: a maturing application for CubeSats, Acta Astronaut. 191 (2022) 394–403, https://doi.org/10.1016/j.actaastro.2021.11.017. ISSN 0094-5765.

[7] I. Iakubivskyi, P. Janhunen, J. Praks, et al., Coulomb drag propulsion experiments of ESTCube-2 and FORESAIL-1, Acta Astronaut. (2019), https://doi.org/10.1016/j.actaastro.2019.11.030. ISSN 0094-5765, http://www.sciencedirect.com/science/article/pii/S0094576519314250.

[8] M. Palmroth, J. Praks, R. Vainio, P. Janhunen, E.K.J. Kilpua, N.Yu. Ganushkina, et al., FORESAIL-1 cubesat mission to measure radiation belt losses and demonstrate de-orbiting, J. Geophys. Res. Space Physics 124 (2019), https://doi.org/10.1029/2018JA026354.

[9] G.-N. Kim, S.-Y. Park, T. Lee, D.-E. Kang, S. Jeon, J. Son, N. Kim, Y.-K. Park, Y. Song, Development of CubeSat systems in formation flying for the solar science demonstration: the CANYVAL-C mission, Adv. Space Res. 68 (11) (2021) 4434–4455, https://doi.org/10.1016/j.asr.2021.09.021. ISSN 0273-1177.

[10] M. Mughal, Smart panel bodies for modular small satellites, in: Aerospace and Electronic Systems Magazine, 29, IEEE, 2014, p. 38, https://doi.org/10.1109/MAES.2014.140127, 41, Dec.

[11] M. Rizwan Mughal, A. Ali, L.M. Reyneri, Plug-and-play design approach to smart harness for modular small satellites, Acta Astronaut. 94 (2) (2014) 754–764, https://doi.org/10.1016/j.actaastro.2013.09.015. FebruaryISSN 0094-5765.

[12] A. Ali, M. Rizwan Mughal, H. Ali, L. Reyneri, Innovative power management, attitude determination and control tile for CubeSat standard NanoSatellites, Acta Astronaut. 96 (2014) 116–127, https://doi.org/10.1016/j.actaastro.2013.11.013. March–AprilPagesISSN 0094-5765.

[13] J. Carlos De Los Rios, D. Roascio, L. Reyneri, C. Sansoè, C. Passerone, D. Del Corso, M. Bruno, A. Hernandez, A. Vallan, ARAMIS: a fine-grained modular architecture for reconfigurable space missions, in: 1st Conference on University Satellite Missions, Rome, 2011, 24 January-01-21.

[14] M.R. Mughal, J.C. De Los Rios, L.M. Reyneri, A. Ali, Scalable plug and play tiles for modular nanosatellites, in: 63rd International Autronautical Congress, Naples Italy, 2012, 1-5 Oct.

[15] M.R. Mughal, A. Ali, L.M. Reyneri, Plug-and-play design approach to smart harness for modular small satellites, Acta Astronaut. 94 (2) (2014) 754–764, https://doi.org/10.1016/j.actaastro.2013.09.015. FebruaryISSN 0094-5765.

[16] S. Speretta, L.M. Reyneri, C. SansoE,M. Tranchero, C. Passerone, Dante Del Corso, Modular Architecture for Satellites, 58th IAC, Hyderabad, India, 24 - 28 September 2007.

[17] T.Y. Kim, Su-Y Chang;, S.S. Yong, Optimizing the design of space radiators for thermal performance and mass reduction, J. Aerosp. Eng. 30 (3) (2017). - May.

[18] Satellite Thermal Control Enginnering, prepared for SME 2004, European Space Agency, ESTEC, Thermal and Structure Division, URL: http://www.tak2000.com/data/Satellite_TC.pdf.

[19] W. Guo, Y. Li, Y.Z. Li, M.L. Zhong, S.N. Wang, J.X. Wang, J.X. Zhang, A self-driven temperature and flow rate co-adjustment mechanism based on Shape-Memory-Alloy (SMA) assembly for an adaptive thermal control coldplate module with on-orbit service characteristics, Appl. Therm. Eng. 114 (2017) 744–755.

[20] T.Y. Kim, Su-Y Chang;, S.S. Yong, Optimizing the design of space radiators for thermal performance and mass reduction, J. Aerosp. Eng. 30 (3) (2017). - May.

[21] D. Park, H.N. K.Miyata, Thermal design and validation of radiation detector for the ChubuSat-2 micro-satellite with high-thermal-conductive graphite sheets, Acta Astronaut. 136 (2017) 387–394.

[22] M. Bonnici, P. Mollicone, M. Fenech, M. Azzopardi, Analytical and numerical models for thermal related design of a new pico-satellite, Appl. Therm. Eng. 159 (2019) 113908.

[23] A. Elweteedy, A. Elmaihy, A. Elhefnawy, Small satellite operational phase thermal analysis and design: a comparative study, INCAS Bulletin 13 (4) (2021) 59–74. Oct 1.
[24] D. Gilmore (Ed.), Satellite Thermal Control Handbook, The Aerospace Corporation Press, El Segundo, CA, 2002.
[25] C. Latham, Technical brief, thermal resistance of interface materials as a function of pressure, J. Elect. Cool. 2 (3) (1996) 35.
[26] P.R. Mashaei, M. Shajryari, Effect of nanofluid on thermal performance of heat pipe with two evaporators; application to satellite equipment cooling, Acta Astronaut. 111 (2015) 345–355.
[27] R. Kovács, V. Józsa, Thermal analysis of the SMOG-1 PocketQube satellite, Appl. Therm. Eng. 139 (2018) 506–513.
[28] I. Grande, A. Sanz-Andrs, C. Guerra, G. Alonso, Analytical study of the thermal behavior and stability of a small satellite, Appl. Therm. Eng. 29 (2009) 2567–2573.
[29] Thermal Analysis and Design Optimization of CubeSats using a Coupled Simulation Tool" by S. E. Kang, Y. S. Kim, and J. H. Lee (2021).
[30] X. Sun, L. Zhou, X. Xu, X. Zhao, J. Huang, Design and test of a novel thermal control system for CubeSats, IEEE Trans. Aerosp. Electron. Syst. 53 (3) (2017) 1288–1299, https://doi.org/10.1109/TAES.2017.2650818.
[31] R. Abellán, J. Viñolas, E. Alarcón, J. Gómez-Elvira, Thermal modeling of a CubeSat with solar panels, Acta Astronaut. 175 (2020) 491–503, https://doi.org/10.1016/j.actaastro.2020.06.027.
[32] P.S. Girão, D.X. Viegas, H.G. Silva, V.M. Gomes, Thermal modeling and simulation of a 6U CubeSat in different orbital environments, Acta Astronaut. 162 (2019) 600–613, https://doi.org/10.1016/j.actaastro.2019.06.035.
[33] A. Ali, K. Ullah, H.U. Rehman, I. Bari, L.M Reyneri, Thermal characterisation analysis and modelling techniques for CubeSat-sized spacecrafts, Aeronaut. J. 121 (1246) (2017) 1858–1878, https://doi.org/10.1017/aer.2017.108.
[34] D. Silva, Modeling the transient response of thermal circuits, Appl. Sci. 12 (2022) 12555, https://doi.org/10.3390/app122412555.
[35] Z. Wang, Q. Qin, Y. Sun, G. Han, H. Ren, Retrieval of surface albedo based on BRDF model, in: IGARSS 2018 - 2018 IEEE International Geoscience and Remote Sensing Symposium, Valencia, 2018, pp. 8949–8952, https://doi.org/10.1109/IGARSS.2018.8518775.
[36] T. He, S. Liang, D. Wang, Q. Shi, X. Tao, Estimation of high-resolution land surface shortwave albedo from AVIRIS data, IEEE J. Selected Topics in Appl. Earth Observat. Remote Sens. 7 (12) (2014) 4919–4928, https://doi.org/10.1109/JSTARS.2014.2302234. Dec.
[37] Y. Song, X. Wang, S. Bi, J. Wu, S. Huang, Effects of solar radiation, terrestrial radiation and lunar interior heat flow on surface temperature at the nearside of the Moon: based on numerical calculation and data analysis, Adv. Space Res. 60 (5) (2017) 938–947. Issue1 SeptemberPages.
[38] A. Ali, J. Tong, H. Ali, M.R. Mughal, L.M. Reyneri, A detailed thermal and effective induced residual spin rate analysis for LEO small satellites, IEEE Access 8 (2020) 146196–146207. Aug 6.